Stretching and folding sustain microscale chemical gradients in porous media

Joris Heyman, Daniel Robert Lester, Régis Turuban, Yves Méheust, Tanguy Le Borgne

Stretching and folding sustain microscale chemical gradients in porous media

Heyman J.[a,1], **Lester D. R.**[b,2], **Turuban R.**[a,3], **Méheust Y.**[a,4], **and Le Borgne T.**[a,5]

[a]Univ Rennes, CNRS, Géosciences Rennes, UMR 6118, 35000 Rennes, France.; [b]School of Engineering, RMIT University, 3000 Melbourne, Victoria, Australia.

This manuscript was compiled on April 19, 2020

Fluid flow in porous media drives the transport, mixing and reaction of molecules, particles and microorganisms across a wide spectrum of natural and industrial processes. Current macroscopic models that average pore-scale fluctuations into an effective dispersion coefficient have shown significant limitations in the prediction of many important chemical and biological processes. Yet, it is unclear how three-dimensional flow in porous structures govern the microscale chemical gradients controlling these processes. Here we obtain high-resolution experimental images of microscale mixing patterns in three-dimensional porous media and uncover an unexpected and general mixing mechanism that strongly enhances concentration gradients at pore-scale. Our experiments reveal that systematic stretching and folding of fluid elements are produced by grain contacts, through a mechanism that leads to efficient microscale chaotic mixing. These insights form the basis for a general kinematic model linking chaotic mixing rates in the fluid phase to the generic structural properties of granular matter. The model successfully predicts the resulting enhancement of pore-scale chemical gradients, which appear to be orders of magnitude larger than predicted by dispersive approaches. These findings offer new perspectives for predicting and controlling the vast diversity of reactive transport processes in natural and synthetic porous materials, beyond the current dispersion paradigm.

Porous Media | Mixing | Lagrangian Chaos

Introduction

Fluid mixing in porous media plays a key role in a range of natural and industrial systems (1–3). In these confined environments, mixing enables or limits reactions controlling the degradation of contaminants in the subsurface, the cycles of biogeochemical elements such as nitrogen, iron and carbon, and the sequestration of CO_2 in deep reservoirs (4–10). Mixing also shapes the nutrient landscapes and chemical gradients seen by bacteria evolving in soils or medical systems (11, 12) and facilitates chemical processes in drug delivery, packed bed reactors, flow batteries, or catalysts (13–15). Increasing evidence of sustained chemical gradients and incomplete mixing below the pore-scale, along with associated impacts upon chemical reactions (3, 16–18), have questioned the relevance of macroscopic dispersion coefficients to capture these processes (1). Yet, it is currently unknown how three-dimensional flow topologies in porous structures control microscale mixing rates and concentration gradients.

Recent theories (19, 20) have suggested that laminar flow through three-dimensional porous media may possess the basic ingredients for chaotic advection, which would represent a possible mechanism for the enhancement of microscale chemical gradients, and the persistence of incomplete mixing at the pore-scale. These chaotic dynamics may have particularly important consequences for microbial processes, a broad range of which are hosted in porous environments (21). Biological processes in turbulent flows have been shown to be deeply altered by chaotic advection, which promotes coexistence of competitive microbial species (22) and affects the chemotactic responses of micro-organisms (23). However, whether such chaotic dynamics can spontaneously develop in laminar flows through porous media remains on open question.

A key experimental barrier to the direct imaging of solute advection in three-dimensional porous materials is their predominantly opaque nature. Whilst X-ray micro-tomography technologies have progressed significantly (24), they still cannot resolve the fine structures produced below pore-scale. In contrast, use of visible spectrum refractive index matching between the solid and the fluid phases represents a viable alternative to observe solute mixing, as obtained with hydrogel beads in water (25). However, as molecular diffusion eventually masks the deformation of dyed fluid elements, a direct measurement of fluid deformation in random porous media is an outstanding challenge. Here we overcome these limitations by performing high-resolution laser imaging of the evolution of a low diffusivity fluorescent dye plume through a column of optically transparent borosilicate spheres via high precision refractive index matching (Fig. 1). This technique allows reconstruction of the three-dimensional dye plume at unprecedented resolution, thus providing direct experimental observation of pore-scale fluid deformation and mixing in

Significance Statement

Porous media flows are central to environmental, industrial, and biological systems, where they transport molecules, particles, and microorganisms and trigger important bio-geo-chemical reactions. There is increasing evidence that many of these processes are highly sensitive to chemical gradients below the pore-scale. But it is unknown how porous architectures control microscale concentration heterogeneities. Here, we provide high-resolution experimental images that fully resolve 3D pore-scale mixing dynamics. We show that grain contacts control the folding of fluid elements in the pore-space, which, in addition to fluid stretching as stagnation points, leads to the exponential enhancement of microscale concentration gradients. We use these insights to derive a kinematic model linking mixing rates to pore geometry, opening new perspectives for reactive transport modelling.

J.H did the experiments, the data analysis and model and wrote the paper. D.R.L. and Y.M. contributed to data and model interpretation and redaction. RT performed the numerical simulations discussed in section A of the S.I. T.L.B formulated the idea and contributed to analysis, interpretation and redaction.

The authors declare no competing interests.

[1]Joris Heyman. E-mail: joris.heymanuniv-rennes1.fr

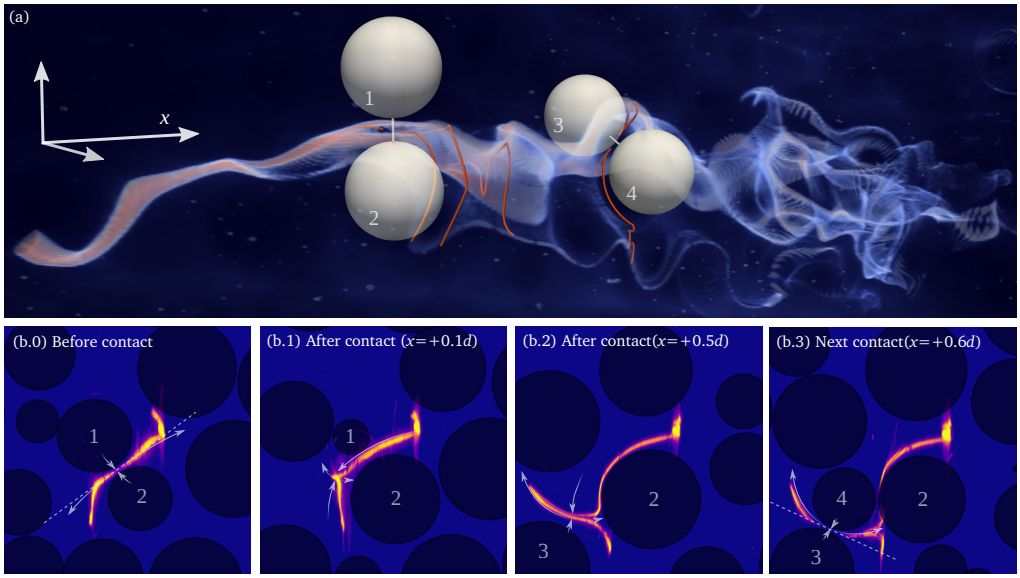

Fig. 1. (a) Experimental dye plume with backbone filament (red lines) at selected stages of the folding mechanism (run III, *SI Video* S4). Beads have been shrunk by 40% and white lines depict the contact line joining bead centres; surrounding beads are not shown. (b) Cross-sections detailing the typical folding stages (run I, *SI Video* S3). Upon passing the contact point 1-2 (b.0), the filament is stretched (diverging arrows) along the contact plane (dashed line) and compressed in the perpendicular direction (converging arrows). After contact (b.1), the directions of stretching and compression are inverted, and a cusp forms, creating a fold (b.2) which is advected over the subsequent contact 3-4 (b.3). Other experimental runs and numerical simulations are reported in *SI Figures* S1, Fig. S2 and *SI Video* S5.

porous media. These novel data reveal the hitherto unknown role of grain contacts in controlling folding and stretching of fluid elements, a mechanism that generates strong chaotic advection and significantly enhances chemical gradients at the microscale. Since grain contacts are inherent to all granular porous materials, we deduce that chaotic mixing is ubiquitous in flow through all such materials, potentially impacting a large range of fluid-borne phenomena in natural and engineered systems.

3D imaging of mixing patterns in porous media

We observed three-dimensional fluid deformation and solute mixing in laminar flows through monodispersed random bead packs of diameters $d = 7, 10$ and 20 mm, optically matched into a glycerol-water fluid mixture (Fig. 5). A fluorescent dye is continuously injected upstream of the transparent column as a thin tube of radius $L_0 \ll d$ (Fig. 2a), and advected downstream by the porous flow at the mean longitudinal advection velocity u. Cross-stream concentration patterns of the dye plume are imaged in the pore-space via a translational scan using a laser sheet and a camera. The dye cross-section rapidly evolves into a highly elongated (Fig. 2b) and striated filamentous structure (Fig. 2c) due to transverse stretching and folding of fluid elements in pores (*SI Videos* S1,S2,S3). The combination of a highly viscous fluid mixture and a high molecular weight dye results in laminar flows of low diffusivity, characterized by Reynolds numbers on the order of $\mathrm{Re}{=}7{\cdot}10^{-3}$ and Péclet numbers on the order of $\mathrm{Pe}{=}10^4$ (*SI Table* S1). The deformation of the dye plume (Fig. 1a) thus closely shadows that of the advected fluid, facilitating direct visualization of pore-scale fluid deformation. We use spline fitting on the images to reconstruct the backbone of the cross-sectional dye footprint, called a filament, and estimate its total length $L(x)$ for 9 to 14 bead diameters downstream from the injection point (see Fig. 2, *SI Video* S3).

The mean total filament elongation L/L_0, averaged over the 18 statistically equivalent packings (*SI Table* S1), exhibits clear exponential growth with normalized longitudinal distance x/d (Figure 3). The dimensionless exponent $\mu \equiv \ln(L/L_0)/(x/d) = 0.29 \pm 0.01$ is independent of both bead diameter and flow rate and is known as the *topological entropy* of the flow (26). Via the central limit theorem, μ is related to the mean λ and variance σ_λ^2 of the dimensionless stretching rate (see Methods)

$$\mu = \lambda + \sigma_\lambda^2/2. \qquad [1]$$

The dimensionless parameter λ is also known as the Lyapunov exponent (26), which can be converted into a mean stretching rate per unit time as $\lambda u/d$. In addition to stretching, the filament also undergoes highly localised folding events which result in closely foliated striations (Fig. 2c). These fluid deformations are the hallmarks of chaotic mixing, and permit thus permitting exponential elongation of material elements in a finite-sized domain.

The role of grain contacts in folding

Folding of dye filaments is consistently initiated downstream of contact points between two beads (Fig. 1b and *SI Figure* S1). The cusp-shaped geometry near grain contacts means that when crossing a contact point (b.0), fluid elements are first compressed in the direction joining the two bead centres and stretched in the perpendicular direction. Downstream of the contact point, the direction of compression and stretching are exchanged and a cusp forms locally in the dye filament (b.1). This cusp is stretched in the following pore space, leading to a folded filament made of two straight segments (b.2). This stretching and folding process is repeated sequentially as the folded filament encounters other contact points (b.3), leading to thin solute dye foliations that are the hallmarks of chaotic advection (26) (Fig. 2c).

Recent studies (19, 20) identified the role of separation and reattachment points on open grain boundaries (saddle points) in generating exponential stretching of fluid elements. Here, we uncovered the distinct role of contact points between grains in generating systematic folding of fluid elements. Simulations of laminar flow in periodic bead packings (see *SI Text* section A) show that attracting and repelling stream surfaces (unstable and stable manifolds) produced by these saddles indeed control stretching of material lines in the pore space. We found that these manifolds intersect orthogonally at grain contacts (*SI*

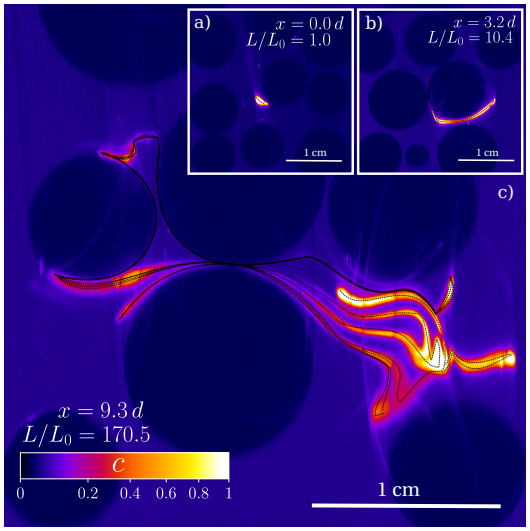

Fig. 2. Cross-stream sections of the fluorescent dye plume at increasing distances from the injection: $x/d = 0$ (a), 3.2 (b) and 9.3 (c)(run II, *SI Video* S1 and S2). Colors represent local dye concentrations. Beads appear in deep blue. A spline curve (dotted black lines) is used to fit the filament backbone on each cross-section image; from which the total filament length L is obtained.

Figure S2 and *SI Video* S5), where both the local flow velocity and the stretching rate vanish and manifold stabilities are exchanged, so that repelling stream surfaces become attracting and vice-versa. Hence, over a contact point, the local flow structure imparts finite curvature to fluid elements, which results in the sharp folds observed experimentally (Fig. 1). The repetition of this basic stretching and folding sequence over successive contact points offers a simple geometric framework to relate stretching rates to granular structure.

Linking stretching statistics to the porous structure

Sharp folding of dye filament in between contact points produces a number n_c of localised cusps of strong curvature, separated by straight segments of moderate curvature (Fig. 6). We define the mean segment length as $L_c = L/n_c$ and the average area swept out by a segment between two successive contact points as $S_c = S/n_c$, where S is the total area swept by the filament. We find that L_c and S_c both converge to stationary values (inset of Figure 3). Hence, the average advection distance between two successive contact points is statistically constant and equal to $X_c = S_c/L_c \approx 3.45\,d$. Over this distance, a single elementary segment folds, giving rise to two new straight elementary segments. Thus, over the same distance, its length $\ell(X)$ must doubles to maintain $\langle \ell \rangle = L_c$ constant, so that $\ell(X) = 2^{(X/X_c)}$. Hence, the average dimensionless stretching rate λ of elementary fluid segments can be estimated as

$$\lambda \equiv \frac{\mathrm{d}(\log \ell)}{\mathrm{d}(X/d)} = \frac{\log 2}{X_c/d} \approx 0.21. \qquad [2]$$

This rate is larger than found in synthetic porous media, such as random pore networks ($\lambda \approx 0.12$ (19)) and body centered cubic assemblies of spheres ($\lambda \approx 0.128$ (27)), reflecting the remarkably efficient stretching and folding process occurring in random granular media. The variance of the stretching rate can be estimated from Eq. (1) as $\sigma_\lambda^2 \approx 0.16$, a value

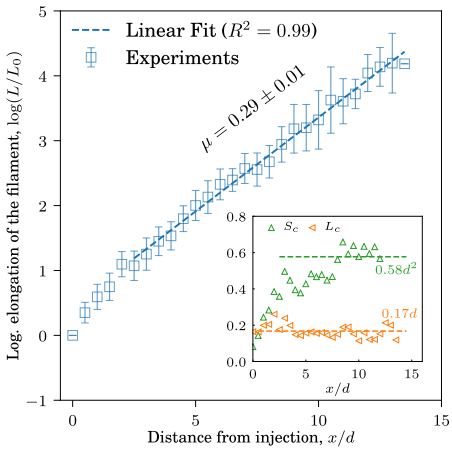

Fig. 3. Total filament elongation L/L_0 with respect to the normalized pore advection distance x/d from the dye injection point. Inset: Convergence of the mean segment length $L_c = L/n_c$ and area $S_c = S/n_c$ toward constant values, with n_c, the number of cusps.

comparable to the mean stretching rates λ, as it is typically the case in space-filling chaotic flows (28).

As shown by Eq. (2), the strength of chaotic advection is entirely governed by the spatial frequency X_c^{-1} with which segments encounter grain contacts. We show in Methods that in isotropic packings $X_c \approx 8 \log 2 \phi z_c d_p/3$, with z_c the coordination number (the mean number of contacts per bead), ϕ the solids volume fraction and d_p the mean pore diameter. This yields a simple geometric estimate of the dimensionless Lyapunov exponent

$$\lambda \approx \frac{3}{8}\frac{\phi z_c d_p}{d}. \qquad [3]$$

Equation 3 is applicable to non-isotropic packings with a prefactor that quantifies the distribution of orientations of the contact lines joining bead centres with respect to the mean flow direction (see Methods). Insertion of the experimental values $z_c = 6$, $\phi = 0.5$ and $d_p/d = 0.24$ in Eq. (3) yields $\lambda \approx 0.27$ which is in reasonable agreement with the experimental estimate of 0.21, given the slight anisotropic nature of our experimental packings (see Methods). Equation 3 provides the first quantitative link between microscopic fluid stretching rates and porous media structural properties.

Discussion

Stretching and folding sustain microscale chemical gradients. Repeated sequences of stretching and folding leads to exponential compression of fluid elements that can sustain concentration gradients at the pore-scale (Fig. 2). These concentration gradients are locally controlled byé the balance between diffusive spreading rate (D_m/s^2), with D_m the molecular diffusivity, and the mean compression rate ($\lambda u/d$), which is equal to the stretching rate in steady incompressible flows. These two rates equilibrate at the Batchelor scale

$$s_B = \sqrt{D_\mathrm{m} d/(\lambda u)}, \qquad [4]$$

which represents characteristic length scale of solute concentration fluctuations. Pore-scale mixing is thus characterized by the dimensionless length scale $s_B^* = s_B/d$, which is related to the macroscopic Péclet number $\mathrm{Pe} = ud/D_\mathrm{m}$ as,

$$s_B^* = (\lambda \mathrm{Pe})^{-1/2}. \qquad [5]$$

For $s_B^* > 1$, the length scale of solute concentration fluctuations are larger than the grain diameter and therefore

concentration fields are expected to be well-mixed at the pore-scale. Our estimation of the Lyapunov exponent λ implies that the transition to incomplete pore-scale mixing occurs at Péclet number above 5, values commonly encountered in many natural and industrial contexts (29). This suggests that a broad range of biogeochemical processes are possibly affected by incomplete pore-scale mixing and chaotic advection. From results established on chemical and microbial processes in turbulent and chaotic flows at comparable mixing rates (22, 23), it is possible to anticipate a range of possible effects of chaotic mixing in porous media, including altered effective kinetics and microbial growth dynamics, increased biodiversity and enhanced benefit of sensing. Because they can only develop in three-dimensional topologies under steady conditions (26), these chaotic dynamics are generally absent in quasi two-dimensional microfluidic experiments used to investigate the microscale interactions between flow, concentration gradients, chemical reactions and microbial processes (3, 11, 30). Novel experiments in three-dimensional porous media and new modelling frameworks are thus needed to explore these dynamics.

Microscale mixing model. The experiments in this study have used high Péclet numbers to uncover the rate and kinematics of mixing in porous media. These results may be extended to prediction of macrosocopic mixing rates and concentration statistics at arbitrary Peclet numbers via lamellar mixing models that couple stretching and diffusion (31–33). In *SI Text* section C, we derive such mixing model and compare its predictions in terms of dye concentration statistics to the experimental data. The lamellar model successfully captures the measured exponential decay of the mean maximum solute concentration of dye filaments with longitudinal distance $c_{\max} \sim \exp(-(\lambda+\sigma^2/2)x/d)$ (Fig. 4), as well as the growth of concentration fluctuations caused by variability of the Lagrangian stretching history. These predictions provide an independent validation of the estimated mean and variance of the stretching rate, $\lambda \approx 0.21$ and $\sigma_\lambda^2 \approx 0.16$. In contrast, conventional mixing models based upon macroscopic dispersion coefficients (1) ignore incomplete mixing at the pore-scale and predict an algebraic decay of concentrations $c_{\max} \sim (x/d)^{-1/2}$ (*SI Text* section B). From the normalized Batchelor scale (Eq. (5)), pore-scale concentration fluctuations predicted by the lamellar model will persist for all Péclet numbers larger than five. In this range, macroscopic dispersion models fails to resolve pore-scale concentration gradients, leading to incorrect predictions of a broad range of reactive transport dynamics (3, 16–18). Coupling lamellar mixing models with reactive processes is therefore a promising avenue to capture the effect of pore-scale incomplete mixing on biogeochemical dynamics.

Porous materials as mixers. From Eq. (3), the mixing efficiency of steady laminar flows through random bead packs (defined as the ratio of the average stretching rate to the average strain rate) is found to be 3% (*SI Text* section D). This value is comparable to the performance of industrial mixers (26) and an order of magnitude larger than that of micro-fluidic chaotic mixers (34), thus opening new opportunities for exploiting the mixing properties of porous materials. Chaotic advection is known to both increase dispersion

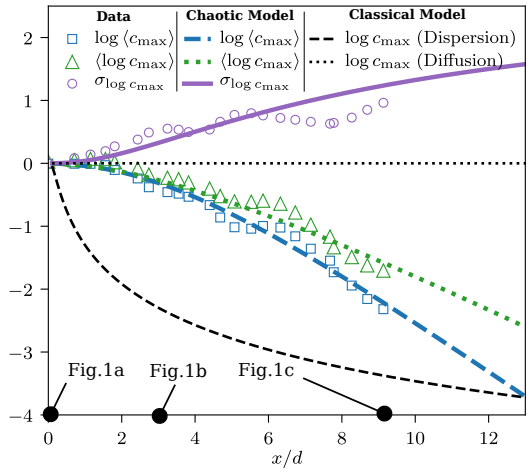

Fig. 4. Experimental average (triangles) and standard deviation (circles) of the local maximum concentration $c_{\max}$ along x. Values are normalized by the initial maximum concentration c_0. Classical model predictions are shown as black dashed and dotted lines. Lamellar mixing model predictions for the average and standard deviation of $c_{\max}$ are shown respectively as the green dotted line and the purple continuous line (see SI Text sections B and C for derivations).

transverse to the mean flow direction and retard longitudinal dispersion (35). It also alters the transport of finite-sized particles such as colloids and micro-organisms (36) and may thus control their clustering in the pore space and deposition on grain boundaries. In relating stretching rates to the porous micro-structure, Eq. (3) offers a possible pathway to the design of engineered porous materials with optimum mixing characteristics. This concept may find important applications in the design of heat exchangers, packed bed filters and reactors, where transverse dispersion and mixing act to enhance process efficiency, and for continuous flow chemistry (15), such as pressure-driven chromatography, where product selectivity and yield strongly depends upon the minimization of longitudinal dispersion. These applications would first require a validation Eq. (3) over a large range of packing geometries.

Conclusions

Using high resolution experimental imaging of microscale mixing in three-dimensional granular media we have demonstrated the existence of efficient stretching and folding of fluid elements at the pore-scale. We use these insights into the kinematics of mixing to develop a stochastic model for the prediction of the Lyapunov exponent from the geometric properties of the grain pack, and validate this model against experimental observations. The formalization of these observations into a chaotic mixing model, coupling stretching and diffusion, demonstrates that incomplete mixing persists at pore-scale for Péclet numbers above five. This model captures the processes governing microscale chemical gradients, opening new perspectives for understanding, predicting and controlling a large spectrum of physical, chemical, and biological processes, in natural and engineered porous systems.

The discovery of systematic and efficient chaotic mixing in single phase laminar flows through random bead packs—the archetype of porous media—calls for deeper investigation of this phenomenon in a broad range of systems, including polydisperse packings, consolidated soils and rocks, and more

complex flows, such as multiphase, inertial or non-Newtonian flows. While these cases may act to modify the rate of mixing, the fundamental kinematics described in this study should persist as they arise from basic fluid-grain interactions. The investigation of these system-specific modulations of chaotic mixing in porous matter form promising research perspectives.

Materials and Methods

Experimental protocol. The porous column consists of a vertically-oriented rectangular column of cross section 48×48 mm (Fig. 5), containing monodisperse borosilicate glass beads (Sigmund Lindner GmbH) of diameter $d = 7{,}10$ or 20mm that are loosely and randomly packed via gravitational settling. The pore space between the beads is filled with a glycerol-water mixture (1.4%w/w water) at controlled temperature (T=25°C). Fluid flow is driven by a constant pressure difference imposed between the inlet and outlet ports, respectively at the top and bottom of the column. The flow rate is continuously monitored at the outlet by a scale. Together with the knowledge of the packing porosity, this provides an estimate of the mean pore velocity, u. To visualize fluid flow and deformation through the bead pack, a solute fluorescent dye (PromoFluor-488LSS) is continuously injected in the upper part of the cell through a needle of internal diameter $L_0 = 0.5\,\mathrm{mm}$. The injected dye develops into a steady plume downstream of the injection point. The mean flow velocity u is chosen to be sufficiently low to get small Reynolds numbers and laminar flows (Re$= ud/\nu \approx 5 \cdot 10^{-3} \ll 1$, where $\nu \approx 700$ cP is the kinematic fluid viscosity), and fast enough for the dye Péclet number to be large and for fluid deformation to be measured from the dye backbone (Pe$= ud/D_\mathrm{m} \approx 8.6 \cdot 10^3$, where $D_\mathrm{m} \approx 2 \cdot 10^{-11}$ m^{2}s^{-1} is the molecular diffusivity of the dye in the glycerol-water mixture). For representativeness, experiments are repeated for multiple dye injection locations and for various packing realisations and bead diameters, as summarised in *SI Table* S1. The coordinates of the bead centres are determined via a three-dimensional Hough transform on the image stack obtained by the translational laser scan, where the background fluid fluorescence allows distinguishing the grains. From these coordinates, several structural properties of the porous media are obtained : ϕ , the solid volume fraction (the ratio of volume occupied by the beads over the total column volume); z_c, the coordination number (the number of neighbouring beads whose centres lie $d \pm 5\%$ away from the reference bead); d_p, the mean diameter of the largest sphere inscribed in the pore space, obtained by a distance transform computed on a voxelized image of the fluid phase.

Reconstruction of the dye filament backbone. In each cross-stream section of the solute dye plume, a one-dimensional backbone of the dye filament is reconstructed via the adjustment of spline curves and its total length L is computed (Fig.2 and Fig. 6a). In experimental run II (Fig. 2 and *SI Video* S1), the tracking is possible until downstream distance $x = 9.27\,d$ (beyond which the diffusive filament merges with itself), corresponding to a total elongation of $L/L_0 \approx 167$ (Fig.2c), where L_0 is the initial length of the dye filament backbone.

Distribution of elongations. The sequential stretching and folding process leading to exponential growth of the total filament backbone length L implies that the length l of a fluid element follows a multiplicative random process (28, 32), such that l grows as $\mathrm{d}l/\mathrm{d}x^* = \gamma l$, where $x^* = x/d$ and γ is a random, statistically stationary *stretching rate* of mean λ and variance σ_λ^2. The length l thus results from the product of the successive stretching rates γ, such that $\log l$ is the sum of a series of independent and identically distributed random variables. From the central limit theorem, the distribution of $\log l$ must then converge with downstream distance towards a normal distribution of mean $\lambda x'$ and variance $\sigma_\lambda^2 x^*$. This convergence is obtained after a few bead diameters since i) the dye filaments length increase exponentially and thus sample an increasingly large number of independent stretching rates in the pore space and ii) the stretching rates are distributed within pores, so that several independent stretching rates are experienced over a unit diameter distance. The mean value of l is thus such that $\langle l \rangle \sim \exp(\mu x^*)$ with $\mu = \lambda + \sigma_\lambda^2/2$, which sets the growth rate of the total filament length to $\langle L/L_0 \rangle = \exp(\mu x^*)$.

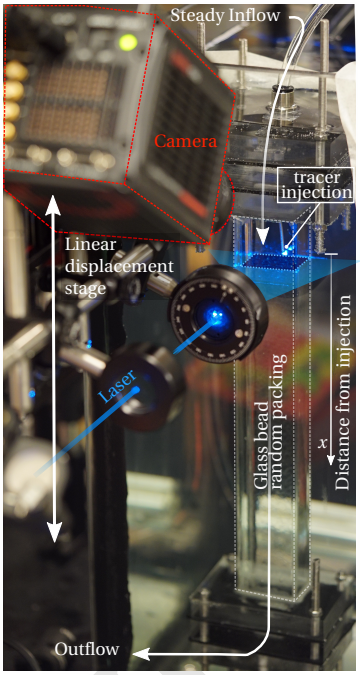

Fig. 5. Experimental setup for three-dimensional imaging of the mixing of a fluorescent solute dye in optically matched porous bead packs. The dye is continuously injected through a thin needle upstream of the granular column, while maintaining a steady background laminar flow. After stabilisation of the solute dye plume, transverse cross-sections of concentrations are obtained by displacing a laser sheet (Oxxius, wavelength 488 nm, beam waist 50 µm) in the x direction while recording the emmited fluorescence with a CMOS camera (Hamamatsu ORCA-Flash4.0 16bits) mounted with a band pass filter (Midopt BN532) and oriented at an angle of 45 degrees from the laser plane. The perspective view is then ortho-rectified by a projective transform.

Number of high curvature regions. As shown in Fig. 1b, when the filament is advected through contact points between beads, localized regions of very high curvature develop in the filament backbone. We define cusps as isolated regions of the filament backbone where the curvature κ of the spline curve exceeds the threshold $\kappa = 10^3 d^{-1}$. We find (Fig. 6c) that the total number n_c of cusps in the filament backbone increases exponentially with the downstream distance x/d at a rate similar to that of the total filament length L. This suggests that stretching and folding events occurs in proportion of each other and that the resulting process is statistically stationary.

Prediction of the mean stretching rates from the porous media properties. Based on the consistently observed sequence of stretching and folding in the pore space and its control by grain contacts (Fig. 1), we derive a general expression for the magnitude of the Lyapunov exponent in random granular media as a function of the coordination number z_c, the solid volume fraction ϕ, the grain diameter d and the mean pore diameter d_p. Since segment lengths must double, on average, each times the segment encounters a contact, that is for each distance X_c, the Lyapunov exponent can be derived from equation Eq. (2) as $\lambda = d \log 2 / X_c = d \log 2 / (S_c/L_c)$, which requires estimating the mean segment length L_c and the mean surface area S_c swept by segments between successive contact points. A geometric estimate for the mean segment length L_c is obtained by assuming that an individual segment doubles its length at the constant exponential rate λ until it reaches the mean pore diameter d_p where it inevitably collides with a contact point located at X_c downstream, e.g. $L_c(x) = d_p/2 \exp(\log 2\, x/X_c)$. This expression yields the average value

$$L_c \approx \frac{d_p}{2 \log 2}. \qquad [6]$$

From tomographic reconstruction of all the experimental runs, the average pore diameter is $d_p \approx 0.24\,d$ (see Methods). Thus, we estimate $L_c \approx 0.17d$ which is in excellent agreement with the observations (Fig. 3). To develop an estimate of S_c, we consider the volume density ρ_V of contact points in the three-dimensional bead pack. As the number of grains per unit volume is $6\phi/(\pi d^3)$ and there are $z_c/2$ independent contacts per grain, the volume density of contact points is then $\rho_V = 3\phi z_c/(\pi d^3)$. Conversely, S_c is equal

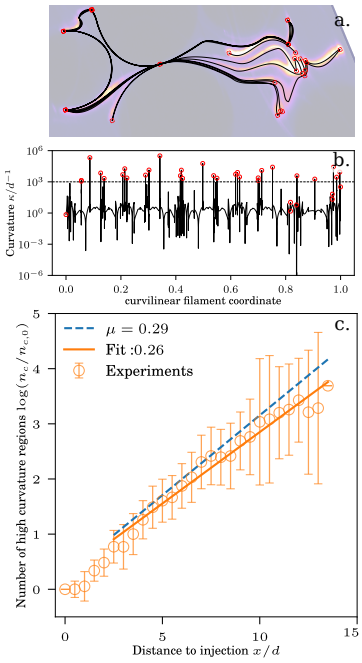

Fig. 6. a. Reconstruction of filament backbone (black line) from dye distribution and localisation of high curvature regions (red circles). b. Local curvature along the filament backbone (black line) with isolated cusps (red circles) and threshold value $\kappa = 10^3 d^{-1}$ for cusp detection (dashed line). Note that the end-points of filaments are considered as cusps, explaining why red circles can exist below κ. c. Exponential growth of the number (n_c) of cusps in the filament backbone as a function of the advection distance (x/d) from the injection point. The fitted exponent for n_c (grey line) is similar to that for the total filament length (dashed line), suggesting stationarity of the stretching and folding processes.

to the inverse of the areal density ρ_A of contact points in a filament sheet. To develop a relationship between ρ_V and ρ_A, we consider a series of filament sheets that arise from continuously injected line sources and extend along length Z in the cross-stream z-coordinate of the column, and are advected over distances X. These series of injection lines are also distributed along distance Y in the other cross-stream y-direction. If we consider the average number n_V of contact points in the volume $V = XYZ$, then the number n_A of contact points contained within a filament sheet is $n_A = \bar{\ell}/Y n_V$, where $\bar{\ell}$ is the average span of filament sheet in the y-direction that pass through a common contact point. The simplest estimate for $\bar{\ell}$ is obtained by considering the behaviour of filament sheets in a open laminar flow over two spheres in contact at an angle α with the mean flow direction x. From symmetry arguments, the horizontal span $\ell(\alpha)$ is given by the projection in the plane normal to x of the contact line connecting the two sphere centres. Thus $\ell(\alpha) = d \sin\alpha$, and $\bar{\ell}$ is given by the mean of $\ell(\alpha)$ over the distribution of contact angles. As $\rho_V \equiv n_V/(XYZ)$ and $\rho_A \equiv n_A/(XY)$, then $\rho_A = \bar{\ell}\rho_V$. For isotropic packings, contact lines are uniformly orientated in the space, and α is distributed as $p(\alpha) = \sin\alpha$. Averaging over this distribution then yields $\bar{\ell} \equiv \overline{d \sin\alpha} = d\pi/4$. From the results above, S_c for isotropic packings is then estimated as

$$S_c = 1/\rho_A = \frac{\pi d^3}{3\bar{\ell}\phi z_c}. \qquad [7]$$

For anisotropic packings the distribution of contact orientations may deviates from $\sin\alpha$, thus yielding different values for $\bar{\ell}$. Eq. (7) and Eq. (6), provide the value of the mean fold distance $X_c = S_c/L_c$ and from Eq. (2), the Lyapunov exponent reads

$$\lambda = \bar{\ell}\frac{3\phi z_c d_p}{2\pi d^2}. \qquad [8]$$

Using the estimates of ϕ, z_c and d_p obtained from tomographic reconstruction and $\bar{\ell}/d = \pi/4 \approx 0.78$ for isotropic packings, equation Eq. (8) yields $\lambda = 0.27$, a value comparable to the experimental estimate ($\lambda = 0.21$). The slight overestimate of λ can be explained by the anisotropy introduced by the gravitational packing of the beads and the finite size of the experimental column. Indeed, independent measurements of $\rho_V = 2.86 d^{-3}$ and of $S_c = 0.58 d^2$ (Fig. 3) indicate that, experimentally, $\bar{\ell}/d = (d\rho_V S_c)^{-1} \approx 0.6$, instead of $\bar{\ell}/d = 0.78$ expected for isotropic packings. Using this value in Eq. (8) yields $\lambda \approx 0.21$, in much better agreement with the experimental estimate.

ACKNOWLEDGMENTS. This research was funded by the Europe Research Council grant ReactiveFronts (648377), ANR project Subsurface mixing and reactions (ANR-14-CE04-0003) and CPER project BUFFON. We thank J. Jimenez-Martinez and B. Geraud for their contributions in the early experimental design and construction.

1. Dentz M, Le Borgne T, Englert A, Bijeljic B (2011) Mixing, spreading and reaction in heterogeneous media: A brief review. *J. Cont. Hydrol.* 120-121:1–17.
2. Rolle M, Le Borgne T (2019) Mixing and reactive fronts in the subsurface. *Reviews in Mineralogy and Geochemistry* 85(1):111–142.
3. Valocchi AJ, Bolster D, Werth CJ (2019) Mixing-limited reactions in porous media. *Transport in Porous Media* 130(1):157–182.
4. Kitanidis PK, McCarty PL (2012) *Delivery and mixing in the subsurface: processes and design principles for in situ remediation.* (Springer Science & Business Media) Vol. 4.
5. Gomez-Velez JD, Harvey JW, Cardenas MB, Kiel B (2015) Denitrification in the mississippi river network controlled by flow through river bedforms. *Nature Geoscience* 8(12):941–945.
6. Datta S, et al. (2009) Redox trapping of arsenic during groundwater discharge in sediments from the meghna riverbank in bangladesh. *Proceedings of the National Academy of Sciences* 106(40):16930–16935.
7. Matter JM, et al. (2016) Rapid carbon mineralization for permanent disposal of anthropogenic carbon dioxide emissions. *Science* 352(6291):1312–1314.
8. Szulczewski ML, MacMinn CW, Herzog HJ, Juanes R (2012) Lifetime of carbon capture and storage as a climate-change mitigation technology. *Proc. Natl. Acad. Sci.* 109(14):5185–5189.
9. Stegen JC, et al. (2016) Groundwater–surface water mixing shifts ecological assembly processes and stimulates organic carbon turnover. *Nature communications* 7:11237.
10. Bochet O, et al. (2020) Iron-oxidizer hotspots formed by intermittent oxic–anoxic fluid mixing in fractured rocks. *Nature Geoscience* pp. 1–7.
11. Borer B, Tecon R, Or D (2018) Spatial organization of bacterial populations in response to oxygen and carbon counter-gradients in pore networks. *Nat. Commun.* 9(1):769.
12. Drescher K, Shen Y, Bassler BL, Stone HA (2013) Biofilm streamers cause catastrophic disruption of flow with consequences for environmental and medical systems. *Proceedings of the National Academy of Sciences* 110(11):4345–4350.
13. Anglin EJ, Cheng L, Freeman WR, Sailor MJ (2008) Porous silicon in drug delivery devices and materials. *Adv. Drug Deliver. Rev.* 60(11):1266–1277.
14. Braff WA, Bazant MZ, Buie CR (2013) Membrane-less hydrogen bromine flow battery. *Nature communications* 4(1):1–6.
15. Meirer F, Weckhuysen BM (2018) Spatial and temporal exploration of heterogeneous catalysts with synchrotron radiation. *Nature Rev. Mater.* p. 1.
16. Gramling CM, Harvey CF, Meigs LC (2002) Reactive transport in porous media: A comparison of model prediction with laboratory visualization. *Environ. Sci. Technol.* 36(11):2508–2514.
17. Berkowitz B, Dror I, Hansen SK, Scher H (2016) Measurements and models of reactive transport in geological media. *Reviews of Geophysics* 54(4):930–986.
18. Wright EE, Richter DH, Bolster D (2017) Effects of incomplete mixing on reactive transport in flows through heterogeneous porous media. *Physical Review Fluids* 2(11):114501.
19. Lester DR, Metcalfe G, Trefry MG (2013) Is chaotic advection inherent to porous media flow? *Phys. Rev. Lett.* 111(17):174101.
20. Turuban R, Lester DR, Le Borgne T, Méheust Y (2018) Space-group symmetries generate chaotic fluid advection in crystalline granular media. *Phys. Rev. Lett.* 120(2):024501.
21. Whitman WB, Coleman DC, Wiebe WJ (1998) Prokaryotes: the unseen majority. *Proc. Natl. Acad. Sci.* 95(12):6578–6583.
22. Tel T, de Moura A, Grebogi C, Károlyi G (2005) Chemical and biological activity in open flows: A dynamical system approach. *Phys. Rep.* 413:91–196.
23. Stocker R (2012) Marine microbes see a sea of gradients. *Science* 338:6107.
24. Boon M, Bijeljic B, Niu B, Krevor S (2016) Observations of 3-D transverse dispersion and dilution in natural consolidated rock by x-ray tomography. *Adv. Water Resour.* 96:266 – 281.
25. Kree M, Villermaux E (2017) Scalar mixtures in porous media. *Phys. Rev. Fluids* 2(10):104502.
26. Ottino J (1990) Mixing, chaotic advection, and turbulence. *Annu. Rev. Fluid Mech.* 22:207–253.
27. Turuban R, Lester DR, Heyman J, Borgne TL, Meheust Y (2019) Chaotic mixing in crystalline granular media. *J. Fluid Mech.* 871:562–594.
28. Meunier P, Villermaux E (2010) The diffusive strip method for scalar mixing in two dimensions. *J Fluid Mech.* 662:134–172.
29. Cushman JH (2013) *The physics of fluids in hierarchical porous media: Angstroms to miles.* (Springer Science & Business Media).
30. de Anna P, et al. (2013) Mixing and reaction kinetics in porous media: an experimental pore scale quantification. *Environ. Sci. Technol.* 48(1):508–516.
31. Le Borgne T, Dentz M, Villermaux E (2013) Stretching, coalescence and mixing in porous media. *Phys. Rev. Lett.* 110:204501.
32. Le Borgne T, Dentz M, Villermaux E (2015) The lamellar description of mixing in porous media. *J. Fluid Mech.* 770:458–498.
33. Lester DR, Dentz M, Le Borgne T (2016) Chaotic mixing in three-dimensional porous media. *J. Fluid Mech.* 803:144–174.
34. Stroock AD, et al. (2002) Chaotic mixer for microchannels. *Science* 295(5555):647–651.
35. Jones S, Young W (1994) Shear dispersion and anomalous diffusion by chaotic advection. *J. Fluid Mech.* 280:149–172.
36. Ouellette NT, O'Malley P, Gollub JP (2008) Transport of finite-sized particles in chaotic flow. *Phys. Rev. Lett.* 101(17):174504.